JOURNAL OF SYNCHROTRON RADIATION

ISSN 1600-5775

Received 25 October 2018
Accepted 29 January 2019

Edited by I. Lindau, SLAC/Stanford University, USA

Keywords: XFEL; X-ray optics; grating diffraction.

On-line monitoring of the spatial properties of hard X-ray free-electron lasers based on a grating splitter

Wenqiang Hua,[a] Guangzhao Zhou,[a] Zhe Hu,[a,b] Shumin Yang,[a] Keliang Liao,[c] Ping Zhou,[a] Xiaohao Dong,[a] Yuzhu Wang,[a]* Fenggang Bian[a]* and Jie Wang[a]*

[a]Institute of Shanghai Applied Physics, Chinese Academy of Sciences, Shanghai 201204, People's Republic of China, [b]University of Chinese Academy of Sciences, Chinese Academy of Sciences, Beijing 100049, People's Republic of China, and [c]Institute of High Energy Physics, Chinese Academy of Sciences, Beijing 100049, People's Republic of China. *Correspondence e-mail: wangyuzhu@sinap.ac.cn, bianfenggang@sinap.ac.cn, wangjie@sinap.ac.cn

X-ray free-electron lasers (XFELs) play an increasingly important role in addressing the new scientific challenges relating to their high brightness, high coherence and femtosecond time structure. As a result of pulse-by-pulse fluctuations, the pulses of an XFEL beam may demonstrate subtle differences in intensity, energy spectrum, coherence, wavefront, *etc*., and thus on-line monitoring and diagnosis of a single pulse are required for many XFEL experiments. Here a new method is presented, based on a grating splitter and bending-crystal analyser, for single-pulse on-line monitoring of the spatial characteristics including the intensity profile, coherence and wavefront, which was suggested and applied experimentally to the temporal diagnosis of an XFEL single pulse. This simulation testifies that the intensity distribution, coherence and wavefront of the first-order diffracted beam of a grating preserve the properties of the incident beam, by using the coherent mode decomposition of the Gaussian–Schell model and Fourier optics. Indicatively, the first-order diffraction of appropriate gratings can be used as an alternative for on-line monitoring of the spatial properties of a single pulse without any characteristic deformation of the principal diffracted beam. However, an interesting simulation result suggests that the surface roughness of gratings will degrade the spatial characteristics in the case of a partially coherent incident beam. So, there exists a suitable roughness value for non-destructive monitoring of the spatial properties of the downstream beam, which depends on the specific optical path. Here, experiments based on synchrotron radiation X-rays are carried out in order to verify this method in principle. The experimental results are consistent with the theoretical calculations.

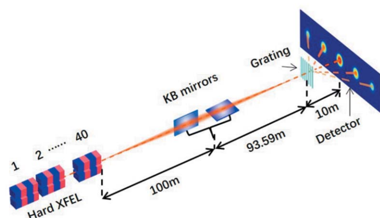

© 2019 International Union of Crystallography

1. Introduction

Hard X-ray free-electron lasers (XFELs) (McNeil & Thompson, 2010), like the LCLS (Bostedt *et al.*, 2016), SACLA (Huang & Lindau, 2012) and the European XFEL (Tschentscher *et al.*, 2017), enabled by developments in electron accelerator technology, generate nearly full spatial and temporal coherent and 1 fs ultrafast X-ray pulses which is many orders of magnitude brighter than the brightest synchrotron source. The unique properties offered by the hard XFEL sources have led to a variety of groundbreaking, innovative experimental techniques, such as coherent diffraction imaging and serial femtosecond crystallography (Abbamonte *et al.*, 2015). These experiments do not only rely on the unique time structure and the peak power of the X-ray pulses but also on the high degree of coherence and the clean well defined wavefront (Barty *et al.*, 2009; Pardini *et al.*, 2017; Rutishauser *et al.*, 2012). However, the XFEL pulses produced from self-amplified spontaneous emission (SASE) or self-

seeded operation exhibit intrinsic pulse-by-pulse fluctuations in temporal properties (pulse energy, spectral content) and spatial profile (intensity, coherence and wavefront, degree of polarization) (Abbamonte *et al.*, 2015). Furthermore, potential performance degradations associated with deformation and vibration introduced by huge transient thermal loads on beam-intercepting components also exist (Tschentscher *et al.*, 2017). Since all these fluctuations can affect measurements performed at XFELs, both *in situ* diagnostics tools and coherence-preserving optical elements have been developed to monitor and to counteract these beam degradations.

Diagnostics devices for machine tuning can often be destructive to the beam whereas diagnostics for experimental operation must (nearly) transparently characterize the FEL pulses. The LCLS single-shot beam profile measurement based on X-ray scintillation and optical imaging (albeit destructive) is capable of revealing imperfections of any upstream X-ray optics such as mirrors and monochromators. The beam centroid position can be monitored non-destructively for hard X-rays at the LCLS using quadrant detection from Compton scattering (Feng *et al.*, 2011). Coherence properties of individual femtosecond pulses of an XFEL beam have been typically measured using Young's experiment in 'diffract and destroy' mode (Vartanyants *et al.*, 2011) and the diffraction method based on Hanbury Brown and Twiss interferometry (Gorobtsov *et al.*, 2018). Wavefront measurements have been achieved through traditional Hartmann-type sensors (Bernhard *et al.*, 2010), grating interferometry (Rutishauser *et al.*, 2012; Kayser *et al.*, 2014, 2017) and speckle tracking (Berujon *et al.*, 2017) or by measuring coherent scattering from well characterized nanoparticles (Loh *et al.*, 2013), although these techniques are destructive, thus providing only typical or 'average' information on the beam wavefront. As presented by Makita *et al.* (2015), an on-line spectrometer for hard XFELs has been developed based on a nanostructured diamond diffraction grating and a bent crystal analyzer. A beam-splitter grating was placed in the direction of the X-ray beam to divert a small portion of the XFEL pulse onto a bending-crystal spectrometer and to transmit the rest of the pulse to be used for experimental purposes. It provides high spectral resolution, interferes negligibly with the XFEL beam, and can withstand intense hard X-ray pulses at high repetition rates of >100 Hz.

In this paper, apart from the configuration of the on-line spectrometer, we present the analysis feasibilities of on-line monitoring of spatial properties of hard XFEL beams based on the grating splitting method. On the basis of theoretical simulation and experimental demonstration, the equivalency of the spatial properties of the zeroth-order and the first-order grating diffracted beams were proven; therefore monitoring the first-order beam is equal to monitoring the transmitted zeroth-order direct beam. The grating-based method has advantages of high X-ray beam transmission and radiation hardness, but in our beamline optical setup it may introduce beam degradation when the grating RMS roughness is >200 nm. Using this non-destructive on-line monitoring method can provide most of the spatial properties of the hard XFEL beam, including beam profile, position, intensity, coherence and wavefront distribution.

2. Methods

The highly coherent XFEL sources can be described by a finite number of transverse modes using the coherent mode decomposition (CMD) of the Gaussian Schell Model (GSM) (Vartanyants *et al.*, 2010; Vartanyants & Singer, 2010; Singer & Vartanyants, 2014; Hua *et al.*, 2013). For the propagation of the XFEL beam, we used a decomposition of the statistical fields into a sum of independently propagating transverse modes for the analysis of the beam properties of these fields at different distances from the source. The limited number of contributing modes significantly simplified the numerical calculations by reducing the number of variables.

A GSM beam is a particular type of partially coherent wavefield which is usually used to describe the XFEL radiation coherence properties as well as intensity distributions. The cross spectral density (CSD) of a planar GSM source is described by (Mandel & Wolf, 1995)

$$J_S(r_1, r_2, z=0) = \left[I(r_1)\, I(r_2)\right]^{1/2} \mu_{\rm s}(r_2 - r_1), \tag{1}$$

where

$$\begin{aligned} I(r) &= I_{0x}\, I_{0y} \exp\left(-\frac{x^2}{2\sigma_{Sx}^2} - \frac{y^2}{2\sigma_{Sy}^2}\right), \\ \mu_{\rm s}(r_2 - r_1) &= \exp\left[-\frac{(x_2 - x_1)^2}{2\xi_{Sx}^2} - \frac{(y_2 - y_1)^2}{2\xi_{Sy}^2}\right]. \end{aligned} \tag{2}$$

Here, $I(r)$ describes the intensity distribution at the points r_1 or r_2 in the survey plane which is perpendicular to the z direction of the beam propagation. The degree of spatial coherence $\mu_{\rm s}$ depends only on the difference of spatial coordinates r_1 and r_2. I_{0x} and I_{0y} are the positive constants representing the maximum intensity in the respective directions that are set to 1 in this paper. The parameters σ_{Sx} and σ_{Sy} are the root-mean-squared source size in the x and y directions, respectively, and ξ_{Sx} and ξ_{Sy} give the coherence lengths of the source.

The CSD of a partially coherent, statistically stationary field of any state of coherence can be decomposed into the sum of independent coherent modes under very general conditions,

$$J(r_1, r_2) = \sum_{mn} \beta_{mn}\, E_{mn}^*(r_1)\, E_{mn}(r_2), \tag{3}$$

where $E_{mn}(r)$ are eigenfunctions which describe the electric field of X-rays; they are known as the coherent modes and are orthogonal, and they are described by the Gaussian Hermite modes. β_{mn} are the eigenvalues that describe the occupancy in each mode. Accordingly, the modes E_{mn} and their corresponding eigenvalues β_{mn} can be found for the x and y directions, respectively. To simplify the simulation, few numbers of the Gaussian Hermite modes need to participate in the simulation process. The criteria for selecting the coherent mode is that the eigenvalue β_{mn} of the (m,n) mode is

larger than 0.1% of the eigenvalue β_{00} of the fundamental mode. Our simulation demonstrated that the mode selection has little effect on the accuracy of the calculation results and has a greater contribution for improving the computational efficiency. That is, the more coherent the beam is, and the fewer coherent modes that are needed, so the CMD method of the GSM works better, especially for the high-coherent XFEL radiation.

Then, the propagation of the field from the source through free space to the observation plane for each mode can be calculated by utilizing the Huygens–Fresnel principle,

$$E_{mn}(u, z_1) = \int_{\Sigma} E_{mn}(r, z_0)\, P_z(u-r)\, \mathrm{d}r, \tag{4}$$

and the coordinate r is taken in the z_0 plane of the source and the coordinate u is taken in the z_1 observation plane. The integration is made in the source plane. The propagator P_z describes the propagation of radiation in free space. It is defined as

$$P_z(u-r) = \frac{\exp\left[(ik/2z)(u-r)^2\right]}{i\lambda(z_1 - z_0)}. \tag{5}$$

When the hard X-ray beam passes through an optical element such as a grating splitter, the transmitted modes are given by $E_{\rm out} = TE_{\rm in}$, where T characterizes the complex-valued amplitude transmittance function of the optical element. After propagation, the CMD representing the beam properties in the plane of observation is determined by equation (3). Then, the intensity distribution I, coherence property μ and wavefront φ at the observation plane ($z = z_1 - z_0$) can be obtained by

$$\begin{aligned} I_z(r) &= J_z(r, r), \\ \mu_z(\Delta r = r_1 - r_2) &= \frac{J_z(r_1, r_2)}{\left[I_z(r_1)\, I_z(r_2)\right]^{1/2}}, \\ \varphi_{mn,z}(r) &= \text{angle}\left[E_{mn,z}(r)\right]. \end{aligned} \tag{6}$$

Consider the binary transmission grating splitter (Paganin, 2006) sketched in Fig. 1(*a*). The maximum and minimum projected thickness of the grating are taken to be A and B, respectively, with the grating period being equal to L. For simplicity, the widths of the grooves are equally distributed between the grooves (L/2). Adopting (x,y) Cartesian coordinates in the plane of the grating, the thickness function $T(x,y)$ could be written as the projected thickness,

$$T(x, y) = \begin{cases} A, & \text{if } \sin(2\pi x/L) \geq 0, \\ B, & \text{otherwise.} \end{cases} \tag{7}$$

Assume that the grating is made of a single homogeneous isotropic non-magnetic material with known complex refractive index $n_\omega = 1 - \delta_\omega + i\beta_\omega$. The real numbers δ_ω and β_ω quantify the refractive and absorptive properties of the material, respectively, as a function of angular frequency ω of the X-rays.

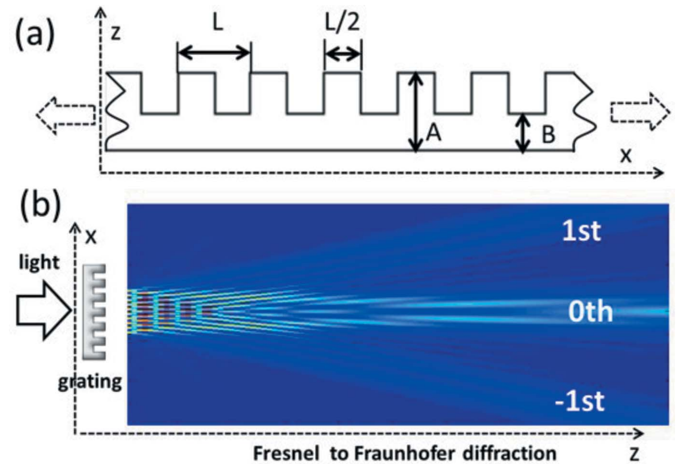

Figure 1
(*a*) Layout of a simple two-level binary diffraction grating in side view. (*b*) Diffraction demonstration when monochromatic plane waves are incident upon the ruled transmission grating.

When a z-directed (normal optic axis perpendicular to the x, y plane) monochromatic partial-coherent hard XFEL beam is incident upon a ruled grating splitter, a series of diffracted orders appears. Here, $k = 2\pi/\lambda$ is the wavenumber associated with monochromatic scalar radiation of wavelength λ. Assuming the grating to be a sufficiently thin optical element and the grating period $L \gg \lambda$, and the projection approximation to be valid, then, for $z = 0$ (*i.e.* the exit surface of the grating), the exit beam can be described as

$$\begin{aligned} E_{{\rm out},\omega}(x, y, z=0) &= E_{{\rm in},\omega}\left\{\exp\left[-2k\beta_\omega T(x,y)\right]\right\}^{1/2} \\ &\quad \times \exp\left[-ik\delta_\omega T(x,y)\right] \\ &= \begin{cases} c_1 = E_0 \exp\left[-kA\left(\beta_\omega + i\delta_\omega\right)\right], & \text{if } \sin(2\pi x/L) \geq 0, \\ c_2 = E_0 \exp\left[-kB\left(\beta_\omega + i\delta_\omega\right)\right], & \text{otherwise.} \end{cases} \end{aligned} \tag{8}$$

To propagate the wavefield $E_{{\rm out},\omega}$ into the vacuum-filled half space $z \geq 0$, equations (4) and (5) should be used for calculating the wavefield downstream of the grating. Then, the spatial properties of the partial-coherent beam can be obtained [equation (3)] and used to calculate the intensity, coherence and wavefront profile at the observation plane.

In light of the preceding analysis, it is clear that the diffraction grating can function as a beam splitter, as indicated in Fig. 1(*b*). Passing through the grating, a normally incident monochromatic beam is split into the various diffracted orders.

In addition to functioning as a beam splitter, equation (8) implies that the transmission grating can also function as a spectrometer. The grating dispersion effect is dependent on the grating period, wavelength and bandwidth. The CVD diamond grating period of 200 nm used by Makita *et al.* (2015) is much larger than the wavelength, 1.24 Å, so the grating dispersion effect is almost negligible when comparing with the crystal spectrometer and will not be discussed here.

Table 1
Simulated beam parameters of a typical hard XFEL beamline using the GSM for a photon energy of 10 keV.

		Analytical calculation†	Numerical simulation	
Source plane at 0 m	Beam size/divergence (μm/μrad)	14.68/0.77	14.68/0.77	
	Transverse coherence length (μm)	54.60	54.60	
Lenses plane at 100 m	Beam size (μm)	77.83	72.93	
	Transverse coherence length (μm)	290	289.14	
	Radius of curvature (m)	Before: 103.67	Before: 104.08	
		After: −96.58	After: −96.53	
Grating/focus plane at 193.59 m	Beam size (μm)	13.84	13.79	
	Transverse coherence length (μm)	52.38	51.40	
	Radius of curvature (m)	∞	∞	
Detector plane at 203.59 m		Without grating	Zeroth order	First order
	Beam size (μm)	16.02	15.94	15.95
	Transverse coherence length (μm)	60.63	59.46	59.46
	Radius of curvature (m)	39.43	38.66	37.85

† From Singer & Vartanyants (2014).

3. Numerical analysis

The GSM method was used to simulate the hard XFEL source SHINE [Shanghai HIgh repetitioN rate XFEL and Extreme light facility (under construction)] (Zhu *et al.*, 2017) whose parameters are specified in Table 1. The propagation of this hard XFEL beamline is sketched in Fig. 2(*a*). The hard XFEL radiation propagated through 100 m of free space, and was focused by a pair of ideal elliptical cylinder KB mirrors which can be considered as an ideal thin lens. For the sake of simulation and illustration, a beam-splitter grating was placed on the focus plane to diffract the beam; the divergence and wavefront of the incident beam and the position of the grating will not change the physical effects of the beam splitting. The downstream observation plane was placed 10 m downstream from the grating and was used to observe the intensity, coherence and wavefront distributions of the split diffraction beams. In this simulation, the selection of the source parameters and beamline layout were considered for typical hard XFEL beamlines and for computational efficiency, and all calculation data based on these will not influence the simulation results.

The beam size and coherence in the beamline expanded and contracted when the beam propagated and focused, and correspondingly the curvature of the wavefront also diverged and converged. The analytical calculation (AC) (Singer & Vartanyants, 2014) method based on the GSM can describe properties of the focused partially coherent X-ray beam, as shown in Table 1. The AC method is based on the results of statistical optics and gives the beam size, wavefront and transverse coherence length at any distance behind an optical element. However, when the optical element is non-ideal (with aberration, slope error and roughness) or unconventional (such as the grating splitter), the AC method is no longer relevant. Therefore, a two-dimensional numerical simulation (NS) method should be developed for calculating

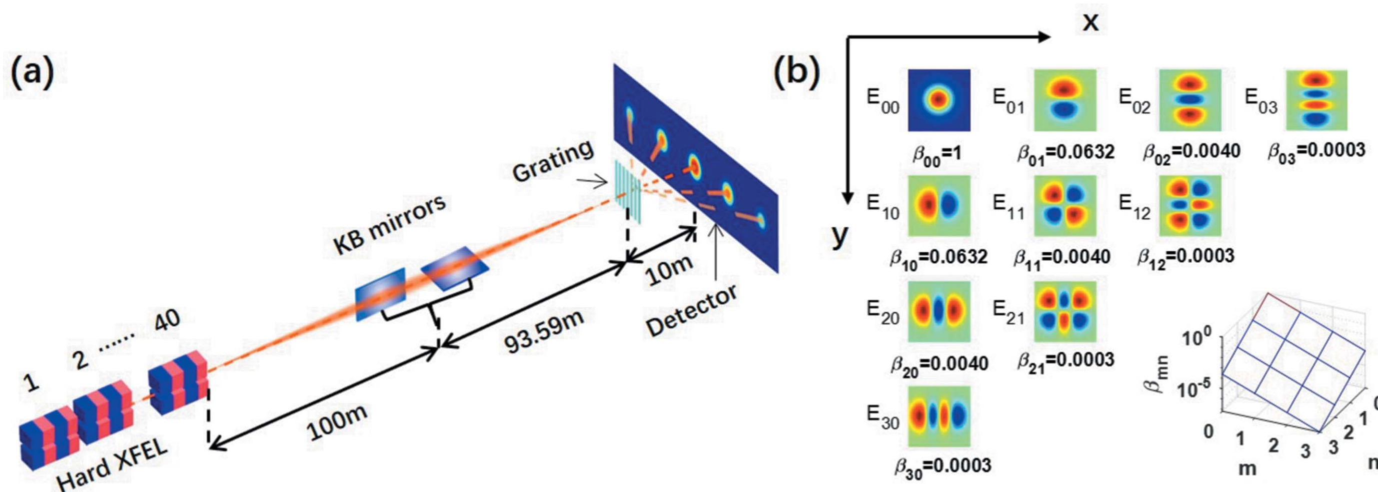

Figure 2
(*a*) Layout of the hard XFEL beamline used in the simulation. (*b*) Ten coherent modes participate in the simulation and their corresponding eigenvalues are illustrated and are larger than 0.01% of β_{00}.

the propagation of a hard XFEL beam for realistic and unusual use.

Based on optic imaging formulae, it should be noted that the focus plane was placed 100 m downstream of the ideal thin lens whose focal length was 50 m. Whereas, according to AC and NS results, the focal plane was moved forward to 93.59 m due to the high coherent beam and diffraction effects (Singer & Vartanyants, 2014).

3.1. Two-dimensional partial-coherent XFEL beam propagation

The two-dimensional NS method was developed based on the CMD method of the GSM and Fourier optics. According to the CMD method of the GSM, only ten coherent modes need to be used in the simulation of a partial-coherent hard XFEL source, as shown in Table 1, and their corresponding eigenvalues were found to be larger than 0.01% of β_{00} as shown in Fig. 2(*b*).

With this NS method, we can simulate the intensity, coherence and wavefront distribution at different places in the beamline, and the optical aberration and distortion can be introduced in arbitrary form. Based on this, we simulated the beam propagation through free space and through focusing lenses as shown in Fig. 3. Comparisons between the NS and the AC method are also specified in Table 1 and Fig. 3, which support the high consistency between the data and the two methods. When only a limited number of ten coherent modes were put into the simulation, a large distortion was found at large $\Delta x, \Delta y$ in the coherence profile due to omitted higher-order coherent modes. So, we introduced a window truncation in the coherence and wavefront calculation, the truncation criteria being that the normalized intensity should be smaller than 1×10^{-4}, which has a small impact on the calculated results.

At the KB mirrors plane, the divergent wavefront was focused into a convergent wavefront, while the intensity and coherent profile behaved consistently across the theoretical ideal thin lenses. Very little wavefront distortion was found at the focal plane due to the near-field Fresnel diffraction at the KB mirrors' focal plane.

As shown in Fig. 2(*a*), a CVD diamond black–white laminar grating splitter with a period of 4 µm and thickness of 4 µm was placed in the KB focal plane to diffract the hard XFEL beam. By employing the NS method, the beam profile diffracted by the grating was calculated and is shown in

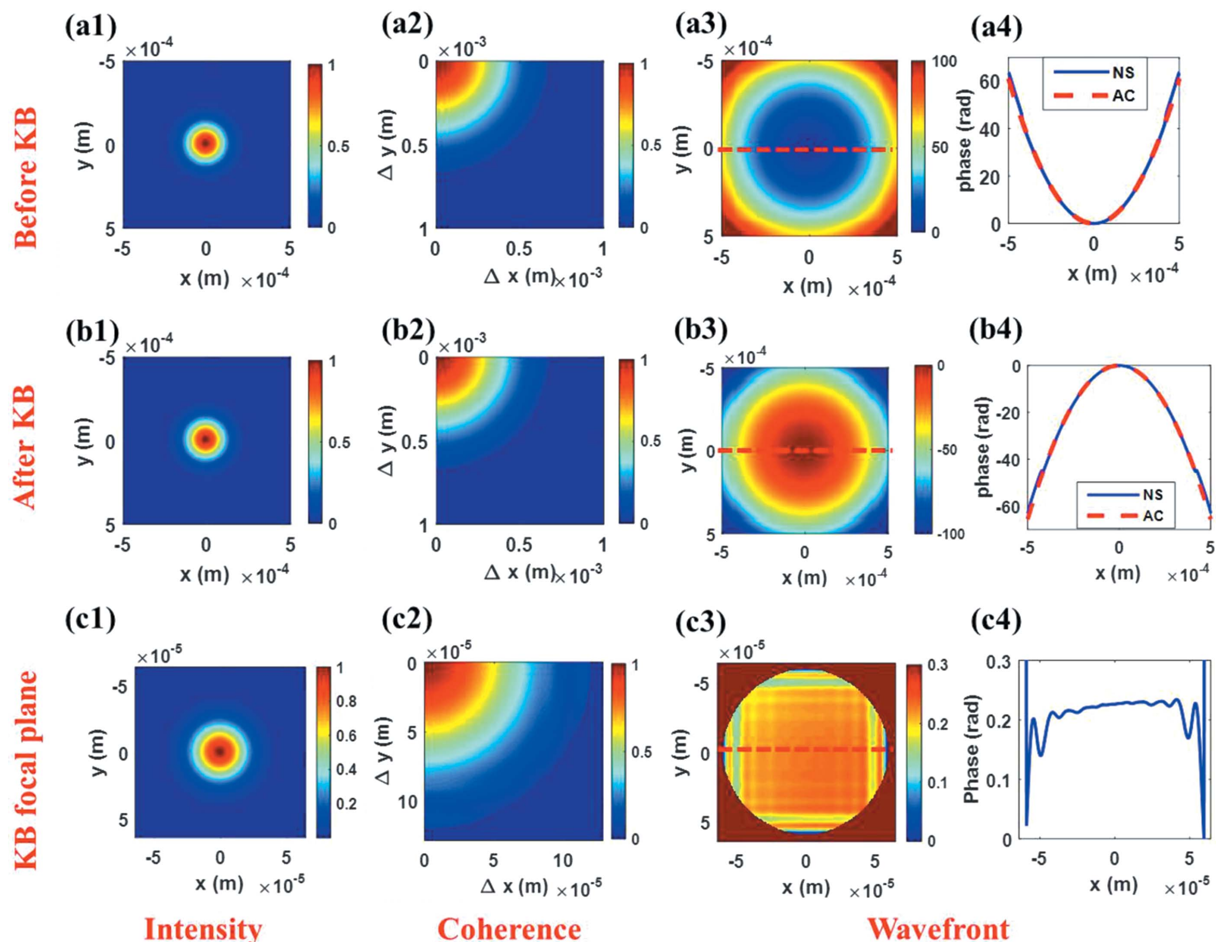

Figure 3
Two-dimensional simulation of the propagation of the partial-coherent XFEL beam. Intensity, coherence and wavefront profiles at the plane (*a*) before the KB mirrors, (*b*) after the KB mirrors and (*c*) in the focal plane of the KB mirrors. Line scans of the wavefront profiles [blue solid line in (*a*3, *b*3, *c*3)] were plotted [blue solid lines in (*a*4, *b*4, *c*4)] and verified by the results of the AC method [red dashed lines in (*a*4, *b*4)].

Fig. 4(*a*), while the transmitted zeroth and diffracted first-order beam spatial properties [Figs. 4(*c*), 4(*d*)] were compared with the transmitted direct beam without the grating [Fig. 4(*b*)]. By using the numerical fitting method, the values of the intensity, coherence and wavefront distribution were kept consistent with each other between the zeroth and the first-order beam as shown in Table 1. The effectiveness of this NS simulation was verified by the AC method. Here, the grating diffraction angle was taken into consideration when calculating the first-order beam's wavefront. Also, the small oscillating parts of the coherence and wavefront profile in Figs. 4(*d*2), 4(*d*3) and 4(*d*4) may be caused by the diffraction angle.

3.2. Beam distortion

To verify the equivalence of the zeroth- and the first-order diffraction beam, amplitude and phase distortion should be introduced to the beam diffraction. As shown in Fig. 5(*a*), a normalized continuous band-limit function was introduced just before the grating and worked as amplitude and phase distortions. Then, the diffracted hard XFEL beam was obtained using the NS method, and the wavy nature of both the amplitude and phase caused obvious distortions in the intensity distribution [see Figs. 5(*b*) and 5(*c*)]. Complete consistency was shown between the zeroth- and the first-order beam.

3.3. Grating roughness

While amplitude and phase distortions can introduce aberrations in the hard XFEL beam, the grating roughness cannot be omitted due to its direct participation in the optical process (Torcal-Milla & Sanchez-Brea, 2011). As demonstrated by Makita *et al.* (2017) and David *et al.* (2011), micrometre-sized phase-shifter gratings contain a rough bottom and smooth top which is caused by the inductively coupled plasma (ICP) assisted reactive ion etching process.

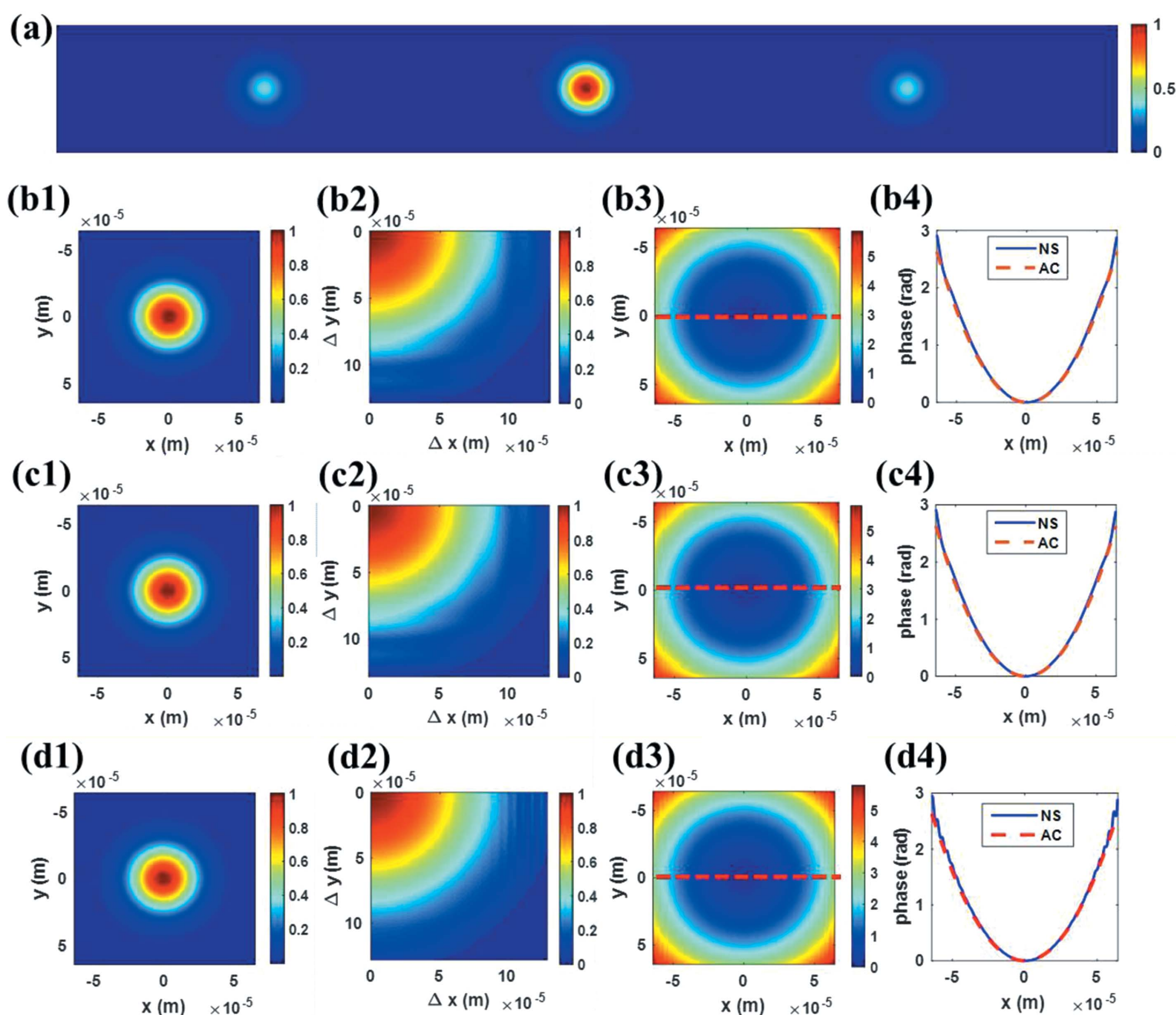

Figure 4
(*a*) Normalized grating diffraction pattern at the detector plane. Intensity, coherence and wavefront profiles of (*b*) the transmitted beam without grating and (*c*) the zeroth-order and (*d*) the first-order beam diffracted by the grating. Line scans of the wavefront profiles [red solid line in (*b*3, *c*3, *d*3)] were plotted [blue solid lines in (*b*4, *c*4, *d*4)] and verified by the results of the AC method [red dashed lines in (*b*4, *c*4, *d*4)].

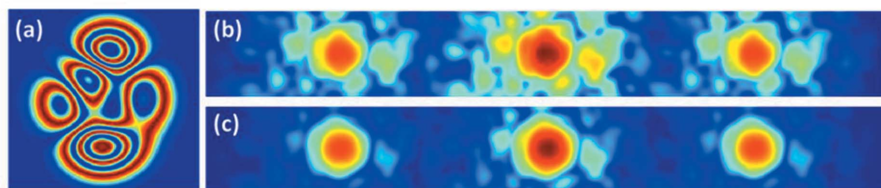

Figure 5
(*a*) Beam amplitude and phase distortion. Intensity profile of the grating diffraction at the detector plane when the incident beam exhibits (*b*) amplitude and (*c*) phase distortion.

The roughness of the bottom of a grating can be represented as a Gaussian random distribution; the RMS roughness of the grating bottom surface is about 100 nm and the correlation lengths are about 500 nm in both two-dimensional orthogonal directions.

To build a similar grating roughness, a two-dimensional random surface height profile was constructed based on the Monte Carlo method,

$$h = F^{-1}\left\{\exp\left[i\phi(f)\right]\left[L\,\mathrm{PSD}(f)\right]^{1/2}\right\},$$
$$\mathrm{PSD}(f) = \lim_{L\to\infty} |F\{h\}|^2/L, \quad (9)$$

where ϕ is a random phase map in normal distribution and satisfies $-\pi < \phi \leq \pi$, and f is a coordinate in the spatial frequency domain. The $F\{\ldots\}$ and $F^{-1}\{\ldots\}$ symbols in (9) represent the fast Fourier transform (FFT) and inverse FFT routines, respectively. The power spectral density (PSD) of the grating height describes the spectral content of the rough surface in the space frequency domain and L is the surface width. For a Gaussian random distribution, the PSD can be described as $\delta^2 l \exp(-f^2 l^2/4)$, where δ is the RMS value of the surface roughness and l is the correlation length.

The simulated rough grating is shown in Fig. 6, where the spatial correlation length and roughness were set to 500 nm and 100 nm, respectively. To investigate the influence of the degree of roughness on the transmitted and diffracted beams, different roughness values (δ = 400 nm, 200 nm 100 nm) were calculated by comparing the spatial properties between the zeroth- and first-order beams (see Fig. 7). Simulation results demonstrated that small distortions can be found in the coherence and wavefront profiles when RMS roughness $\delta >$ 200 nm. As a result, the RMS roughness of this CVD diamond grating splitter used in this beamline layout should be smaller than 200 nm. According to the optical path, there exists a suitable roughness value. When the roughness is lower than this value, the influence on the spatial characteristics can be basically ignored; the roughness and other requirements of the CVD diamond grating and the rest of the optical elements can also be calculated using the NS method.

4. Experiment

The demonstrated experiment was performed on beamline BL19U2, an undulator beamline dedicated to biological small-angle X-ray scattering at the Shanghai Synchrotron Radiation Facility (SSRF), China (Li *et al.*, 2016). A monochromatic beam of 12 keV was provided by a 1.6 m U20 undulator and a Si(111) double-crystal monochromator (DCM). Downstream horizontal (at 31.2 m) and vertical (at 34 m) mirrors focused the X-ray beam onto the detector plane. A secondary source slit at 41 m was used to cut the beam. The spatial coherence properties of the X-ray beam have been measured using a combined method with a pinhole and a grating, and the coherence length was 3.44 µm × 4.76 µm (horizontal × vertical) with a square secondary source opening of 100 µm × 100 µm (Hua *et al.*, 2017). Here a 5 µm pinhole (Zeiss) drilled into a piece of platinum–iridium alloy sheet was used to select the coherent beam which was located 50 m downstream from the source, and a JJ X-ray scattering-free slit, placed 1 m further downstream, was used to block the parasitic scattering. The beam-splitter grating followed closely behind. The experiment used a one-dimensional transmission grating with a period of 282 nm, a line width of 141 nm (see Fig. 8) and an active area of about 120 µm × 120 µm. The grating was fabricated on a low-stress 100 nm Si_3N_4 membrane using lithography (Crestec CABL-9500C). An 80 nm-thick Au layer was deposited by electron-beam evaporation after lithography. A Hamamatsu ORCA-Flash 4.0 LT C11440-42U sCMOS camera (2048 × 2048 pixels with an effective pixel size of 6.5 µm × 6.5 µm) was placed 3.44 m downstream from the grating to allow for a sufficiently large Δy of 1.23 mm, and to separate the diffraction peaks at the camera plane. To obtain low-back-

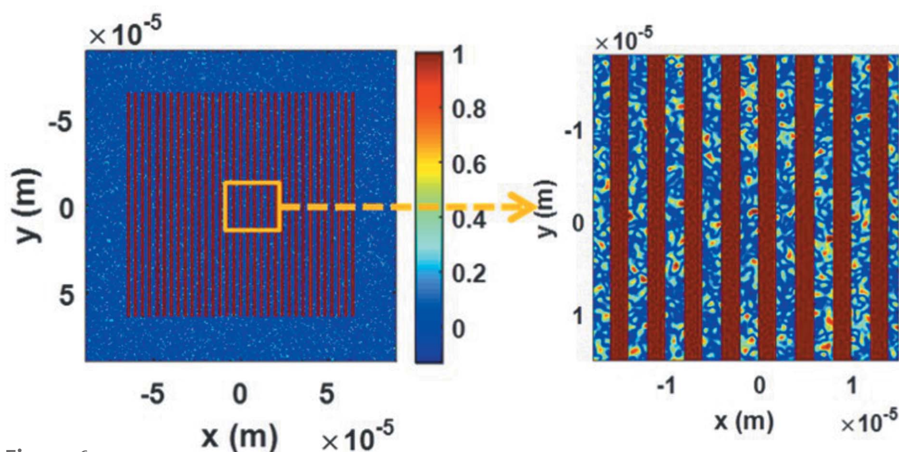

Figure 6
The rough grating used in the simulation (δ = 400 nm and l = 500 nm). The scalar bar was used for both images and demonstrates the percentage of the grating height. An enlarged image is given on the right-hand side as indicated by the orange box and the arrow.

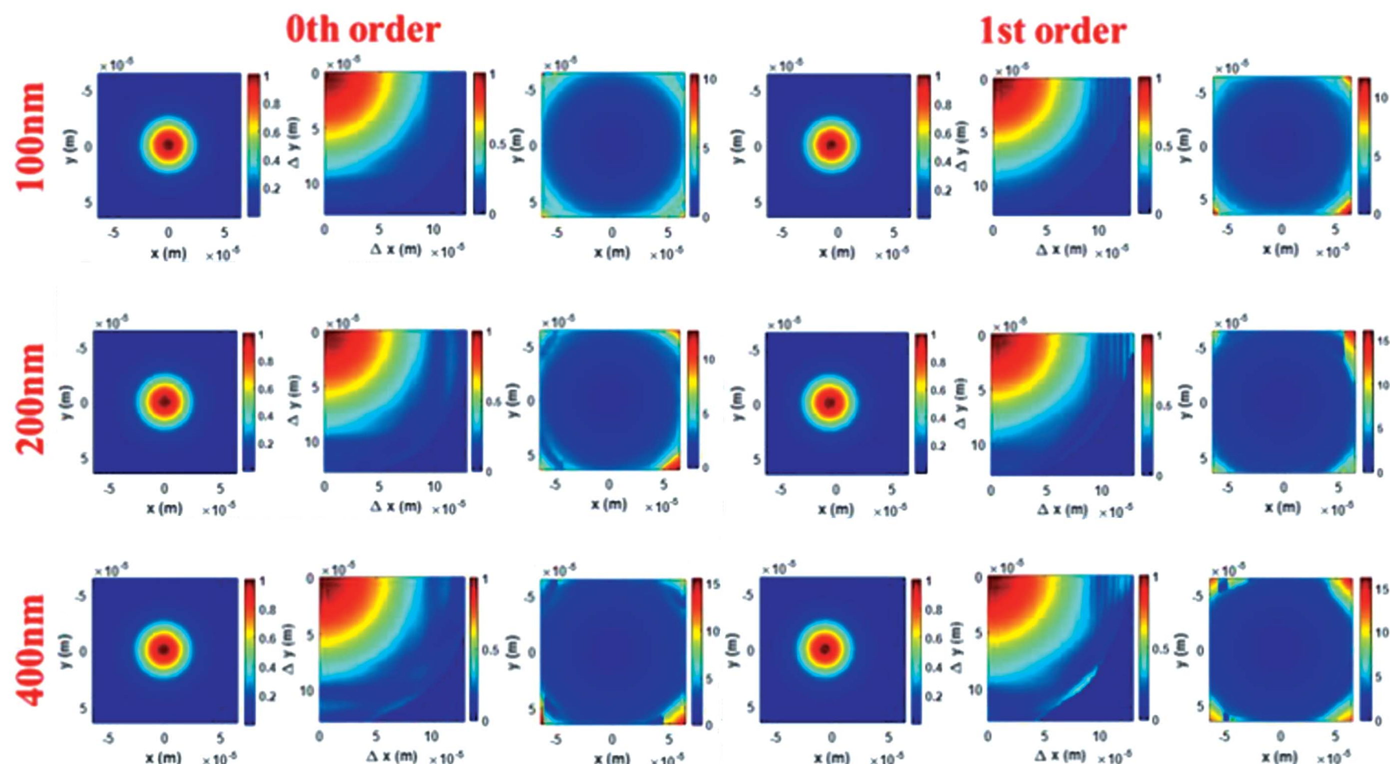

Figure 7
Influence of different grating roughness values (δ = 400 nm, 200 nm 100 nm) on the zeroth and the ±first-order diffraction beam's two-dimensional intensity, coherence and wavefront profiles.

ground data, an evacuated flight tube (sealed by kapton windows) was placed between the grating and the detector to reduce the additional signal due to air scattering. A 200 µm-diameter tungsten bar was used as a beamstop to protect the camera from being damaged and to allow a longer exposure time.

At 12 keV photon energy, the direct beam was almost identical with and without the grating for high transmission and low diffraction, as shown in Figs. 9(*a*1) and 9(*a*2). To calculate the diffraction efficiency, the diffracted ±first-order

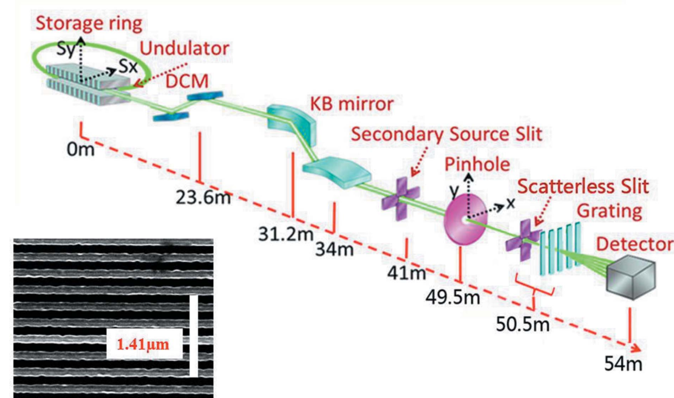

Figure 8
Layout of the grating diffraction experiment performed on the coherent hard X-ray undulator beamline at the SSRF BL19U2. (Left bottom) One-dimensional transmission Au grating with a period of 282 nm, line width of 141 nm used as a beam splitter in the diffraction experiment.

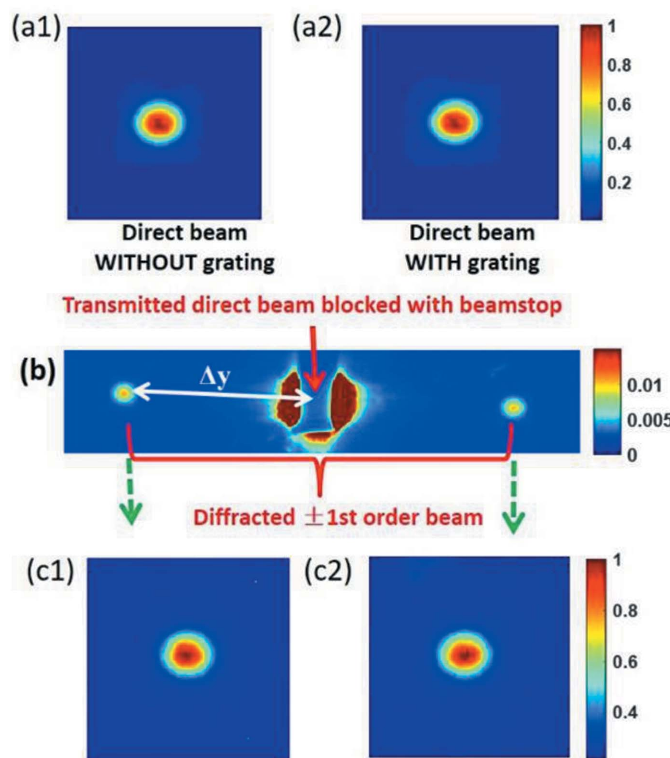

Figure 9
Beam profiles recorded at 12 keV photon energy: (*a*1, *a*2) Direct beam profiles recorded without and with grating. (*b*) Grating diffraction profiles on a log scale, with beamstop. (*c*1, *c*2) Diffracted ±first-order beam profiles.

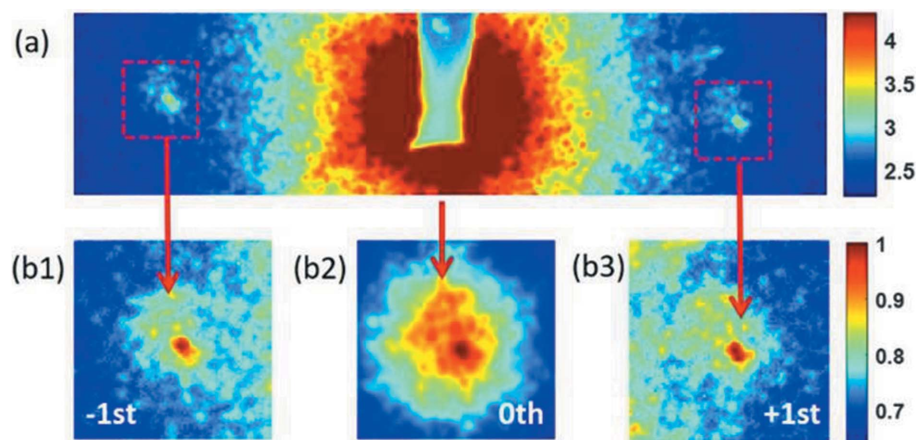

Figure 10
(a) Grating diffraction beam profiles on a log scale, recorded at 12 keV photon energy with grating, paper (working as a diffuser) and beamstop. (b1, b3) Diffracted ±first-order beam profiles on a log scale. (b2) Transmitted zeroth-order direct beam on a log scale.

beam [see Figs. 9(c1) and 9(c2)] contained about 2.17×10^{-8} of the incident beam intensity [see Fig. 9(a1)]. Higher diffraction orders are negligible, resulting in nearly 100% transmission of the zeroth-order diffraction.

To verify the equivalence of the zeroth and the ±first diffracted beam, an emery paper with fine particles was used to introduce random phase. As shown in Fig. 10, strongly distorted speckle was obtained with coherent incident beam, but the diffracted ±first-order beams showed nearly the same profile as the transmitted zeroth-order beam. The visible difference of the first-order diffraction beam may stem from the large scattering range of the zeroth-order beam. Furthermore, the clean speckle pattern with good contrast also proved the high coherence of the incident beam.

5. Conclusion

In summary, we have developed a two-dimensional NS method to calculate the propagation of a highly coherent hard XFEL beam. Compared with the developed AC method, the NS method has almost the same computational accuracy, and it could introduce non-ideal and unconventional optical elements into the beamline. Using this NS method, we calculated the performance of a grating splitter used on a hard XFEL beamline, and verified the equivalence of the spatial properties of the zeroth- and first-order diffraction beam. All the simulation results give a theoretical basis for non-destructive on-line monitoring of a hard XFEL beam's properties, including intensity distribution, coherence and wavefront profile. The demonstrated experiments have also been performed on a SSRF undulator beamline to validate its effectiveness and its versatility, while the intensity distribution, coherence and wavefront profile of the hard FEL X-ray beam were monitored with high transmission, and there is negligible interference with the diffracted beam for analysis.

Acknowledgements

The authors would like to thank all colleagues at beamlines BL19U2 and BL13W1 at the SSRF. The grating was manufactured by the XIL Group of the SSRF.

Funding information

The following funding is acknowledged: National Natural Science Foundation of China (Nos. 11675253, 11505278, U1732123, U1432115).

References

Abbamonte, P., Abild-Pedersen, F., Adams, P., Ahmed, M., Albert, F., Mori, R. A., Anfinrud, P., Aqui-La, A., Armstrong, M. & Arthur, J. (2015). Report SLAC-R-1053. SLAC National Accelerator Laboratory, Menlo Park, CA, USA.

Barty, A., Soufli, R., McCarville, T., Baker, S. L., Pivovaroff, M. J., Stefan, P. & Bionta, R. (2009). *Opt. Express*, **17**, 15508–15519.

Bernhard, F., Pavle, J., Svea, K., Barbara, K., Klaus, M., Elke, P., Bernd, S. & Kai, T. (2010). *New J. Phys.* **12**, 083015.

Berujon, S., Ziegler, E., Cojocaru, R. & Martin, T. (2017). *Proc. SPIE*, **10237**, 102370K.

Bostedt, C., Boutet, S., Fritz, D. M., Huang, Z., Lee, H. J., Lemke, H. T., Robert, A., Schlotter, W. F., Turner, J. J. & Williams, G. J. (2016). *Rev. Mod. Phys.* **88**, 015007.

David, C., Gorelick, S., Rutishauser, S., Krzywinski, J., Vila-Comamala, J., Guzenko, V. A., Bunk, O., Färm, E., Ritala, M., Cammarata, M., Fritz, D. M., Barrett, R., Samoylova, L., Grünert, J. & Sinn, H. (2011). *Sci. Rep.* **1**, 57.

Feng, Y., Feldkamp, J. M., Fritz, D. M., Cammarata, M., Aymeric, R., Caronna, C., Lemke, H. T., Zhu, D., Lee, S., Boutet, S., Williams, G., Tono, K., Yabashi, M. & Hastings, J. B. (2011). *Proc. SPIE*, **8140**, 81400Q.

Gorobtsov, O. Y., Mukharamova, N., Lazarev, S., Chollet, M., Zhu, D., Feng, Y., Kurta, R. P., Meijer, J. M., Williams, G., Sikorski, M., Song, S., Dzhigaev, D., Serkez, S., Singer, A., Petukhov, A. V. & Vartanyants, I. A. (2018). *Sci. Rep.* **8**, 2219.

Hua, W., Bian, F., Song, L., Li, X. & Wang, J. (2013). *Chin. Phys. C*. **37**, 068001.

Hua, W., Zhou, G., Wang, Y., Zhou, P., Yang, S., Peng, C., Bian, F., Li, X. & Wang, J. (2017). *Chin. Opt. Lett.* **15**, 33401–33405.

Huang, Z. & Lindau, I. (2012). *Nat. Photon.* **6**, 505–506.

Kayser, Y., David, C., Flechsig, U., Krempasky, J., Schlott, V. & Abela, R. (2017). *J. Synchrotron Rad.* **24**, 150–162.

Kayser, Y., Rutishauser, S., Katayama, T., Ohashi, H., Kameshima, T., Flechsig, U., Yabashi, M. & David, C. (2014). *Opt. Express*, **22**, 9004–9015.

Li, N., Li, X., Wang, Y., Liu, G., Zhou, P., Wu, H., Hong, C., Bian, F. & Zhang, R. (2016). *J. Appl. Cryst.* **49**, 1428–1432.

Loh, N. D., Starodub, D., Lomb, L., Hampton, C. Y., Martin, A. V., Sierra, R. G., Barty, A., Aquila, A., Schulz, J., Steinbrener, J., Shoeman, R. L., Kassemeyer, S., Bostedt, C., Bozek, J., Epp, S. W., Erk, B., Hartmann, R., Rolles, D., Rudenko, A., Rudek, B., Foucar, L., Kimmel, N., Weidenspointner, G., Hauser, G., Holl, P., Pedersoli, E., Liang, M., Hunter, M. S., Gumprecht, L., Coppola, N., Wunderer, C., Graafsma, H., Maia, F. R. N. C., Ekeberg, T., Hantke, M., Fleckenstein, H., Hirsemann, H., Nass, K., White, T. A., Tobias, H. J., Farquar, G. R., Benner, W. H., Hau-Riege, S., Reich, C., Hartmann, A., Soltau, H., Marchesini, S., Bajt, S., Barthelmess, M., Strueder, L., Ullrich, J., Bucksbaum, P., Frank, M.,

Schlichting, I., Chapman, H. N. & Bogan, M. J. (2013). *Opt. Express*, **21**, 12385–12394.
Makita, M., Karvinen, P., Guzenko, V. A., Kujala, N., Vagovic, P. & David, C. (2017). *Microelectron. Eng.* **176**, 75–78.
Makita, M., Karvinen, P., Zhu, D., Juranic, P. N., Grünert, J., Cartier, S., Jungmann-Smith, J. H., Lemke, H. T., Mozzanica, A., Nelson, S., Patthey, L., Sikorski, M., Song, S., Feng, Y. & David, C. (2015). *Optica*, **2**, 912–916.
Mandel, L. & Wolf, E. (1995). *Optical Coherence and Quantum Optics*. Cambridge University Press.
McNeil, B. W. J. & Thompson, N. R. (2010). *Nat. Photon.* **4**, 814–821.
Paganin, D. M. (2006). *Coherent X-ray Optics*. Oxford University Press.
Pardini, T., Aquila, A., Boutet, S., Cocco, D. & Hau-Riege, S. P. (2017). *J. Synchrotron Rad.* **24**, 738–743.
Rutishauser, S., Samoylova, L., Krzywinski, J., Bunk, O., Grünert, J., Sinn, H., Cammarata, M., Fritz, D. M. & David, C. (2012). *Nat. Commun.* **3**, 947.
Singer, A. & Vartanyants, I. A. (2014). *J. Synchrotron Rad.* **21**, 5–15.
Torcal-Milla, F. J. & Sanchez-Brea, L. M. (2011). *J. Opt. Soc. Am. A*, **28**, 308–313.
Tschentscher, T., Bressler, C., Gruenert, J., Madsen, A. P., Mancuso, A., Meyer, M., Scherz, A., Sinn, H. & Zastrau, U. (2017). *Appl. Sci.* **7**, 592.
Vartanyants, I. A., Mancuso, A. P., Singer, A., Yefanov, O. M. & Gulden, J. (2010). *J. Phys. B At. Mol. Opt. Phys.* **43**, 3535–3537.
Vartanyants, I. A. & Singer, A. (2010). *New J. Phys.* **12**, 035004.
Vartanyants, I. A., Singer, A., Mancuso, A. P., Yefanov, O. M., Sakdinawat, A., Liu, Y., Bang, E., Williams, G. J., Cadenazzi, G., Abbey, B., Sinn, H., Attwood, D., Nugent, K. A., Weckert, E., Wang, T., Zhu, D., Wu, B., Graves, C., Scherz, A., Turner, J. J., Schlotter, W. F., Messerschmidt, M., Lüning, J., Acremann, Y., Heimann, P., Mancini, D. C., Joshi, V., Krzywinski, J., Soufli, R., Fernandez-Perea, M., Hau-Riege, S., Peele, A. G., Feng, Y., Krupin, O., Moeller, S. & Wurth, W. (2011). *Phys. Rev. Lett.* **107**, 144801.
Zhu, Z., Zhao, Z., Wang, D., Liu, Z., Li, R. & Yin, L. (2017). *Proceedings of the 38th International Free Electron Laser Conference (FEL'17)*, 20–25 August 2017, Santa Fe, NM, USA, pp. 182–184. MOP055.